Monthly Notices of the ROYAL ASTRONOMICAL SOCIETY
Royal Astronomical Society
MNRAS **549**, 1–14 (2026)
Advance Access publication 2026 June 08
https://doi.org/10.1093/mnras/stag1072

Three extremely metal-poor stars: discovery of a new CEMP-no star

Partha Pratim Goswami[1]★ and Aruna Goswami[2]★
[1]*Department of Physics, Dakshin Kamrup College, Mirza, Kamrup 781125, India*
[2]*Indian Institute of Astrophysics, Koramangala, Bangalore 560034, India*

Accepted 2026 June 1. Received 2026 June 1; in original form 2026 May 18

ABSTRACT

We have conducted detailed high-resolution spectroscopic studies on three extremely metal-poor (EMP) stars HE 0401−0138, HE 1153−0518, and HE 1246−1344. For the stars HE 0401−0138 and HE 1246−1344, we have estimated the abundances of C, Na, Mg, Ca, Sc, Ti, Cr, Mn, Co, Ni, Sr, and Ba along with the upper limits for Li, O, La, Ce, Pr, Nd, Sm, and Eu. For HE 1153−0518, abundances of seven light elements from C through Ni and two heavy elements, Y and Ba, have been derived, together with upper limits for Li, O, and La. Based on their observed abundance patterns, HE 0401−0138 and HE 1246−1344 are classified as normal EMP stars, whereas HE 1153−0518 is identified as a newly discovered CEMP-no star. HE 1153−0518 shows strong carbon enhancement with a high absolute carbon abundance, extreme sodium enrichment, very low neutron-capture element abundances, and a very low carbon isotopic ratio (^{12}C/^{13}C = 2.0). Its spectral energy distribution shows clear infrared excess, indicating the presence of circumstellar dust. The abundance pattern of HE 1153−0518 suggests enrichment by early nucleosynthetic processes, such as faint core-collapse supernovae with mixing and fallback, while the possibility of binary interaction and subsequent internal mixing cannot be ruled out. The discovery and detailed study of HE 1153−0518 add an important object to the small population of high-A(C) CEMP-no stars and provide valuable constraints on early chemical enrichment pathways and the nature of the first generations of stars.

Key words: stars: abundances – stars: AGB – stars: individual [HE 0401−0138, HE 1153−0518, HE 1246−1344].

1 INTRODUCTION

Extremely metal-poor (EMP) stars, with metallicities [Fe/H] < −3.0 (T. C. Beers & N. Christlieb 2005), are among the oldest known objects in the universe and serve as critical indicators of early Galactic chemical enrichment. Their chemical compositions provide a valuable understanding of the nature of the first stars and the nucleosynthetic processes that took place in the early universe (A. Frebel & J. E. Norris 2015). Driven by large-scale surveys and dedicated follow-up studies (T. C. Beers & N. Christlieb 2005; A. Frebel 2018), the discovery and study of EMP stars have made significant progress over the past few decades. EMP stars are especially important as they retain the chemical signatures of the early universe, having formed from gas that had been only minutely polluted by prior star formation episodes. Among EMP stars, carbon-enhanced metal-poor (CEMP) stars, characterized by [C/Fe] > +0.7 (W. Aoki et al. 2007; P. P. Goswami, R. S. Rathour & A. Goswami 2021), represent a significant fraction (J. Yoon et al. 2016). The CEMP-no subclass, where neutron-capture elements are not enhanced, is thought to have formed from material enriched by the earliest supernovae or by asymptotic giant branch (AGB) stars with minimal *s*-process contributions (J. E. Norris et al. 2013).

As the sample of CEMP stars increased, several studies began to explore their positions in absolute carbon abundance A(C) and [Fe/H] space. The apparent bimodality in A(C) at different metallicities was first noted by (S. Rossi et al. 2005). M. Spite et al. (2013) examined literature abundance data for about 50 CEMP main-sequence turnoff and dwarf stars, including both CEMP-*s* and CEMP-no stars, and reported a clear bimodality in A(C), with stars at [Fe/H] > −3.0, dominated by CEMP-*s* stars, forming a high-carbon plateau at A(C) ≈ 8.25, while stars at [Fe/H] < −3.4, consisting exclusively of CEMP-no stars, occupied a lower region around A(C) ≈ 6.5. P. Bonifacio et al. (2015) confirmed and extended this result using a larger sample, finding a similar separation of CEMP-*s* and CEMP-no stars in A(C)–[Fe/H] space.

Building on these results and using a much larger and more homogenous dataset, J. Yoon et al. (2016) identified three morphological groups in the A(C)–[Fe/H] plane. In this scheme, Group I is dominated by CEMP-*s* and CEMP-*r*/*s* stars with high A(C), while Groups II and III consist primarily of CEMP-no stars. Group II CEMP-no stars show relatively low A(C) and exhibit a clear trend with metallicity, whereas Group III CEMP-no stars display higher A(C) values and do not show any clear metallicity dependence. They also noted the presence of a small number of

★ E-mail: partha.goswami.iiap@gmail.com (PPG); aruna@iiap.res.in (AG)

CEMP-no stars with high A(C) occupying the Group I region, but did not provide a detailed explanation for their origin. Subsequently, J. Yoon et al. (2019) studied the group morphology of CEMP stars in both the Galactic halo and satellite dwarf galaxies and showed that Group I and Group III CEMP-no stars coexist in A(C)–[Fe/H] and A(C)–A(Ba) space. From this behaviour, they suggested that these stars may share a common nucleosynthetic origin, highlighting the complexity of carbon production and early chemical enrichment events.

It is crucial to understand the formation and evolution of EMP and CEMP-no stars in order to reconstruct the early chemical history of the Galaxy and to constrain the nature of their progenitor systems (T. Hansen et al. 2014). In a recent chemodynamical study of two EMP CEMP-no stars HE 1243−2408 and HE 0038−0345 with [Fe/H] ~ -3.05 and -2.92 respectively, J. Shejeelammal & A. Goswami (2024) demonstrated that the objects were likely accreted from dwarf spheroidal (dSph) satellite galaxies, thereby supporting hierarchical assembly scenario of the Galaxy. A detailed analysis of their abundance patterns further indicates that both stars belong to Group II CEMP-no stars, which exhibit a well-defined trend with metallicity. Similarly, a chemical abundance study of the EMP stars HE 2148−2039 and HE 2155−2043 by M. Purandardas & A. Goswami (2021) revealed that HE 2148−2039, with A(C) < 6.28, is a Group II CEMP-no star, whereas HE 2155−2043, with A(C) $\sim$ 7.05 and [Fe/H] < -3.3, belongs to Group III. In contrast to Group II stars, Group III CEMP-no stars do not exhibit a clear dependence on metallicity. These distinct chemical characteristics provide important constraints on the origin and formation pathways of CEMP-no stars. The discovery and detailed abundance analysis of additional CEMP-no stars are therefore essential for refining models of the first stars and for improving our understanding of Galactic chemical evolution.

In this study, we present a detailed high-resolution spectroscopic analysis of three EMP stars: HE 0401−0138, HE 1153−0518, and HE 1246−1344. Our results indicate that one of these objects, HE 1153−0518, is a CEMP-no star, thereby adding to the growing sample of such stars. This new identification contributes to the expanding database of CEMP-no objects and provides an additional probe of early nucleosynthetic processes. The present analysis is expected to support ongoing efforts to constrain the nature of the first stars and to improve our understanding of the chemical evolution of the early Galaxy. Section 2 presents a review of the previous studies on the programme stars available in the literature. The spectroscopic data used in the present work are described in Section 3. In Section 4, we explain the methods adopted to determine the radial velocities and stellar atmospheric parameters. Section 5 outlines the abundance analysis and presents the resulting chemical abundances. A detailed discussion on the chemical peculiarities of the programme stars and their possible formation channels is given in Section 6. Finally, Section 7 summarizes the main conclusions of this study.

2 PREVIOUS STUDIES ON THE PROGRAMME STARS

HE 0401−0138 & HE 1246−1344

P. S. Barklem et al. (2005) presented analysis of 'snapshot' spectra of HE 0401−0138 and HE 1246−1344 among 253 metal-poor halo stars. The spectra were obtained using VLT/UVES in the wavelength range 3760–4980 Å with $R\sim$20 000. As an initial guess of the atmospheric parameters, P. S. Barklem et al. (2005) have considered photometric $T_{\rm eff}$, metallicity estimates from the calibration of the Ca II K line along with B-V colour, log g from log g–$T_{\rm eff}$ correlation (S. Honda et al. 2004), microturbulent velocity (ξ) = 1.8 km s^{-1}, and V_{macro} = 1.5 km s^{-1}. The parameters were then refined using an automated analysis based on the Spectroscopy Made Easy (SME) package by J. A. Valenti & N. Piskunov (1996). P. S. Barklem et al. (2005) derived the abundances of eleven light elements from C through Ni and two heavy elements, Sr and Ba, for both HE 0401−0138 and HE 1246−1344. The abundance of Y is also reported for HE 0401−0138. L. Zhang et al. (2011) adopted the atmospheric parameters from P. S. Barklem et al. (2005) to derive the abundances of C and Si for HE 0401−0138 and HE 1246−1344. J. Ren, N. Christlieb & G. Zhao (2012) derived the upper limit of [Th/Fe] in 77 metal-poor stars, including HE 1246−1344.

HE 1153−0518

Atmospheric parameters and elemental abundances for HE 1153−0518 based on high-resolution spectra ($R \gtrsim 20\,000$) have not been previously reported in the literature. In this work, we present the first detailed abundance analysis of this object using high-resolution ($R \sim 50\,000$) spectroscopy.

The Gaia Collaboration (2023) report an effective temperature of $T_{\rm eff} = 4553.3$ K for this star, which is slightly lower than our estimate. However, their derived surface gravity (log g = 2.18) and metallicity differ significantly from our results. While our analysis identifies HE 1153−0518 as an EMP star with [Fe/H] = −3.08, Gaia Collaboration (2023) report a substantially higher value of [Fe/H] = +0.516. The large discrepancy in [Fe/H] is likely due to the strong impact of molecular carbon bands on the low-resolution *Gaia* spectra used by the GSP-Phot pipeline (M. Lucey et al. 2023). Our measured radial velocity of +72.39 km s^{-1} is marginally lower than the value reported in *Gaia* early DR3 $+76.48 \pm 7.62$ km s^{-1} (Gaia Collaboration 2023). These significant discrepancies in the derived stellar parameters motivated a more detailed investigation of the chemical properties of this star.

3 SOURCE OF SPECTRA

We have obtained high-resolution ($R\sim$ 50 000) spectra of the stars HE 0401−0138, HE 1153−0518, and HE 1246−1344 from the SUBARU archive[1]. The spectra were acquired using the High Dispersion Spectrograph (HDS; K. Noguchi et al. 2002) mounted to the 8.2-m Subaru Telescope of the National Astronomical Observatory of Japan (NAOJ) at the Mauna Kea Observatory in Hawaii. The wavelength range of the spectra is roughly 4020–6775 Å, with a gap of about 100 Å (between 5340 and 5440 Å) caused by the physical separation of the CCD detectors. The detector consists of two 4100 × 2048 EEV CCDs combined, each having 13.5 μ pixels. We used the *continuum* task in the Image Reduction and Analysis Facility (IRAF) to continuum-fit the spectra. Fig. 1 displays the sample spectra of the programme stars in the 5160–5190 Å wavelength range. Table 1 provides the basic information about the programme stars.

[1] http://jvo.nao.ac.jp/portal

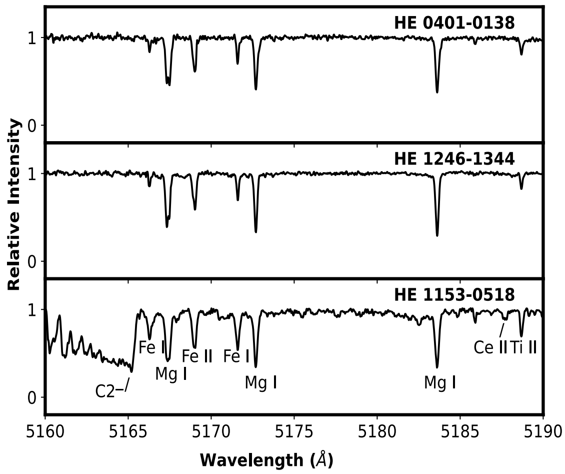

Figure 1. Sample spectra of the programme stars in the wavelength region 5160–5190 Å.

4 RADIAL VELOCITIES AND ATMOSPHERIC PARAMETERS OF THE PROGRAMME STARS

4.1 Radial velocities

To determine the radial velocities of the programme stars, we measured the shifts in the wavelengths of several clean and unblended lines in their spectra. We used the Arcturus spectrum (K. Hinkle et al. 2000) as a template for the laboratory wavelength of the rest frame to ensure homogeneity in the analysis. Arcturus was chosen because it belongs to the giant class and has a temperature comparable to the stars under study. After accounting for heliocentric motion, the calculated mean radial velocities are shown in Table 2 along with the standard deviation from the mean values. We also included literature values for comparison. All three programme stars show variability in radial velocity.

4.2 Photometric temperatures

Based on the infrared flux method (IRFM) colour-temperature calibrations, we have calculated the photometric temperatures of the programme stars using broadband colours, optical, and IR. We used the Two Micron All Sky Survey (2MASS) photometric catalogue (R. M. Cutri et al. 2003) to get the photometric magnitudes for J, H, and K. We calculated the photometric temperatures for the programme stars using the $J-H$ and $V-K$ colours at various assumed metallicity values, as described in our earlier works (A. Goswami et al. 2006; A. Goswami, W. Aoki & D. Karinkuzhi 2015; P. P. Goswami et al. 2021). Table 3 displays the resulting photometric temperatures. Since $T_{\rm eff}(J-K)$ is independent of metallicity (A. Alonso, S. Arribas & C. Martinez-Roger 1996; A. Alonso, S. Arribas & C. Martínez-Roger 1999), we used this temperature as an initial guess to choose the correct model atmosphere through an iterative process.

4.3 Atmospheric parameters from spectral energy distribution fitting

Spectral energy distribution (SEDs) can be used to determine stellar parameters and to examine infrared and ultraviolet excess in stars. We have used the Virtual Observatory SED Analyzer (VOSA; A. Bayo et al. 2008) tool to construct and analyse the SEDs. SEDs are constructed from the observed photometric data points spanning a large wavelength range and then fitted with theoretical models to acquire the required stellar parameters. A detailed discussion of the procedure can be found in S. Rani et al. (2021).

In order to generate the SEDs, we have used the photometric data from VO catalogues (included in VOSA) and the Kurucz atmospheric models (F. Castelli & R. L. Kurucz 2003) corresponding to $[\alpha/\mathrm{Fe}] = +0.4$. The visual extinction (A_V) for the objects has been estimated using the reddening maps provided by E. F. Schlafly & D. P. Finkbeiner (2011). For the object HE 0401−0138, we have used 73 photometric points covering a wavelength range 4010–21590 Å. Atmospheric model with $T_{\rm eff} = 5000$ K, $\log g = 2.5$ and $[\mathrm{Fe/H}] = -4.0$ gave the best fit to the SED (Fig. 2a) of the object. For HE 1153−0518, we have used 11 photometric points covering a wavelength range 4671–46028 Å. Atmospheric model with $T_{\rm eff} = 4750$ K, $\log g = 0.0$ and $[\mathrm{Fe/H}] = -4.0$ gave the best fit to the SED (Fig. 2b) of the object. For HE 1246−1344, we have used 61 photometric points covering a wavelength range 4010–46028 Å. Atmospheric model with $T_{\rm eff} = 5000$ K, $\log g = 0.5$, and $[\mathrm{Fe/H}] = -4.0$ gave the best fit to the SED (Fig. 2c) of the object.

The bottom panels of each subfigure of Fig. 2 show fractional residuals, that is, the ratio of the difference between the observed flux and model flux to that of the observed flux. The fractional residuals for the objects HE 0401−0138 and HE 1246−1344 are close to zero for all data points, which indicates that the model spectra represent the SEDs quite well. However, the fractional residuals of HE 1153−0518 exhibit systematic positive deviations from zero at wavelengths longer than approximately 2 μm. Although the available photometric coverage is limited to only 11 data points, such an infrared excess is not seen in the other two programme stars, whose SEDs are well reproduced by the models over the entire wavelength range. We therefore interpret this deviation as possible evidence for circumstellar dust emission. Nevertheless, a more robust confirmation would require additional mid-infrared photometric observations. The potential astrophysical implications of this excess are discussed in Section 6.

4.4 Spectroscopic determination of atmospheric parameters

We have determined the atmospheric parameters of the programme stars using a set of clean and unblended Fe I and Fe II lines as thoroughly discussed in P. P. Goswami et al. (2021). These lines have excitation potentials ranging from 0.0 eV to 6.0 eV. Table 4 presents the Fe lines, along with the corresponding atomic data and equivalent widths, used for the estimation of the stellar atmospheric parameters.

The atmospheric models (without convective overshooting) were selected from the Kurucz grid of model atmospheres[2] through an iterative process. For the analysis of the stars, we used an updated version of the radiative transfer code MOOG (C. A. Sneden 1973). To choose an initial model atmosphere for a programme star, we used photometric temperature and log g for giants as initial estimates. The conventional methods of excitation potential balance, equivalent width balance, and ionization equilibrium of Fe I and Fe II lines were applied to determine $T_{\rm eff}$, ξ, and log g, respectively. The derived abundances of Fe I and Fe II were used to calculate the metallicity, [Fe/H]. Table 5 presents the

[2] http://kurucz.harvard.edu/grids.html

Table 1. Basic data for the programme stars.

Star name	RA(2000)	Dec.(2000)	*B*	*V*	*J*	*H*	*K*	Exposure (s)	Date of obs.	Spectrograph used	Resolving power
HE 0401−0138	04 03 49.88	–01 30 02.45	14.72	13.84	11.95	11.46	11.30	1800	27-02-2005	HDS/SUBARU	50 000
HE 1153−0518	11 55 54.74	–05 34 48.14	16.50	15.07	13.25	12.71	12.56	1200	28-02-2005	HDS/SUBARU	50 000
HE 1246−1344	12 49 20.25	–14 00 41.59	–	14.39	12.70	12.22	12.05	2700	01-03-2005	HDS/SUBARU	50 000

Table 2. Radial velocities of the programme stars.

Star name	Date of observation	V_r (km s^{-1}) (our estimates)	V_r (km s^{-1}) *a*	V_r (km s^{-1}) *b*
HE 0401−0138	27-02-2005	+70.02±0.22	+137.4	+112.27
HE 1153−0518	28-02-2005	+72.39±0.95	–	+76.48±7.62
HE 1246−1344	01-03-2005	+67.27±0.41	+47.90	+47.28±7.61

Note. a – P. S. Barklem et al. (2005); *b* – Gaia Collaboration (2023)

Table 3. Temperatures from photometry and SEDs.

Star Name	$T_{\rm eff}$ $J-K$)	$T_{\rm eff}$ (−1.5) $(J-H)$	$T_{\rm eff}$ (−2.0) $(J-H)$	$T_{\rm eff}$ (−2.5) $(J-H)$	$T_{\rm eff}$ (−1.5) $(V-K)$	$T_{\rm eff}$ (−2.0) $(V-K)$	$T_{\rm eff}$ (−2.5) $V-K)$	SED fitting	Spectroscopic estimates
HE 0401−0138	4690	4967	4943	4895	4505	4504	4510	5000	4830
HE 1153−0518	4546	4706	4653	4639	4527	4527	4533	4750	4700
HE 1246−1344	4687	4980	4956	4908	4685	4683	4687	5000	4780

Note. The numbers in parentheses below $T_{\rm eff}$ represent the metallicities at which the photometric temperatures are calculated. Temperatures are given in Kelvin.

atmospheric parameters of the programme stars derived from our analysis alongside their literature values. We used the parameters derived from the spectroscopic method for further analysis.

As discussed in Section 2, the atmospheric parameters reported by Gaia Collaboration (2023) for HE 1153−0518 differ markedly from those derived in this work. To assess the reliability of our parameter estimates, we performed spectral synthesis of selected Fe I lines in the observed spectrum. We find that the atmospheric parameters adopted in this study reproduce the observed line profiles satisfactorily, whereas those reported by *Gaia* predict significantly stronger Fe I absorption features that are not supported by the observations (Fig. 3).

5 RESULTS: ABUNDANCE ANALYSIS

We have used the radiative transfer code MOOG 2013 (C. A. Sneden 1973) for conducting the spectroscopic analysis of the programme stars. MOOG operates under the assumptions of Local Thermodynamic Equilibrium (LTE). For deriving the elemental abundances of the stars, both the equivalent width method and spectrum synthesis method have been employed. The excitation potential and log *gf* values for the spectral lines used in the equivalent width method have been taken from the Kurucz database[3] of atomic linelists. The relevant atomic transition data for the lines, along with the measured equivalent widths for a representative set of lines, are provided in Table Table 4. The complete linelist is given in Table A1. The elemental abundances of the programme stars are presented in Tables 6 and 7.

[3]https://lweb.cfa.harvard.edu/amp/ampdata/kurucz23/sekur.html

5.1 Li, carbon, nitrogen, oxygen

Spectral lines due to lithium and oxygen could not be found in any of the three stars. We have estimated the upper limits of the abundances of Li and O for the programme stars using Li I 6708 Å and [O I] 6300 Å lines. We have derived the abundance of carbon in HE 0401−0138 and HE 1246−1344 using spectrum synthesis calculations of the CH band at 4310 Å. Other molecular bands due to carbon are absent in these two objects. For the object HE 1153−0518, the C_2 bands at 5165 Å (Fig. 4) and 5635 Å have been used to derive the abundance of carbon using spectrum synthesis method. While the abundance of carbon is found to be solar in HE 0401−0138 ([C/Fe] = +0.29) and HE 1246−1344 ([C/Fe] = +0.02) HE 1153−0518 exhibits enhancement of carbon with [C/Fe] = +2.86. CN band at 4215 Å could not be detected in the spectra of any objects. So, we could not determine the abundance of nitrogen in the programme stars. The isotopic ratio of carbon, ^{12}C/^{13}C, could be derived only for HE 1153−0518 using the spectrum synthesis calculations of C_2 band at 4740 Å. This particular band is absent in the other two stars. The linelists of

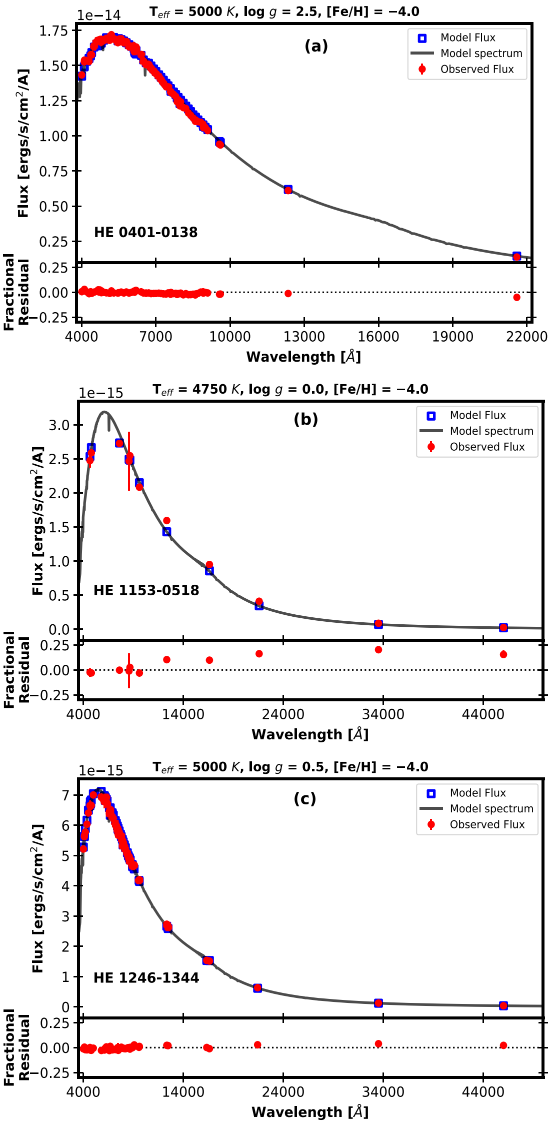

Figure 2. SED fits for the programme stars. The filled circles with error bars represent the observed fluxes at different wavelengths, while the open squares denote the corresponding model fluxes. The solid curves show the best-fitting Kurucz model spectra.

the CH band at 4310 Å and the C_2 bands at 4740 Å, 5165 Å, and 5635 Å are adopted from the *linemake*[4] atomic and molecular line database.

5.2 Light elements

We have derived the abundances of Na, Mg, Ca, Ti, Cr, and Ni for all three programme stars using the equivalent width technique. For Ti, spectral lines due to both the available species Ti I and Ti II have been used to derive the abundances. Both the species yielded abundance consistent with error bars. Usable lines due to Co could not be detected in the spectrum of the star HE 1153−0518. For the other two stars, we could derive the abundance of Co. As Sc and Mn show hyperfine splitting, we used the spectrum synthesis technique to estimate the abundances of Sc and Mn. While Sc II 4246.822 Å & Sc II 4320.732 Å lines are used for HE 0401−0138 and HE 1246−1344, only Sc II 4246.822 Å could be used for HE 1153−0518. We could not detect any good Mn line in the spectrum of HE 1153−0518. For HE 0401−0138, we have used Mn I 4030.753 Å & Mn I 4033.062 Å lines to derive the abundance of Mn. For HE 1246−1344, we have used Mn I 4033.062 Å and Mn I 4766.418 Å lines to derive the Mn abundance. The hyperfine contributions to the Sc and Mn lines are adopted from *linemake*.

5.3 Neutron-capture elements

We have derived the abundances of Sr for HE 0401−0138 and HE 1246−1344. Sr is found to be solar in HE 0401−0138 and subsolar in HE 1246−1344. We could not find any good line due to Sr for the object HE 1153−0518. Abundance of Y has been derived for HE 0401−0138 and HE 1153−0518 and it is found to be solar in both the objects. Abundance of Y could not be derived for the other object due to the absence of clean and usable lines in the spectrum. The absorption lines used for the equivalent width method can be found in Table 4. We have used spectrum synthesis calculations to derive the abundance of Ba for all three objects. For HE 0401−0138, we have used Ba II 6141.713 Å and Ba II 6496.897 Å lines; For HE 1246−1344, we have used Ba II 4554.029 Å line and for HE 1153−0518, we have used Ba II 4554.029 Å, Ba II 5853.668 Å and Ba II 6141.713 Å lines. Ba is found to be sub-solar in all three stars. We could not find any lines due to La, Ce, Pr, Nd, Sm and Eu in any of the objects. However, we have estimated the upper limits of these elements in HE 0401−0138 and HE 1246−1344. We could derive the upper limit of the abundance of La in HE 1153−0518. In Fig. 5, we have compared the abundances (log ϵ) of a few light and heavy elements of our programme stars with that of other metal-poor stars compiled by A. Frebel (2010) from literature. Figs 5 (a) and (b) clearly show that all three programme stars exhibit elemental abundances consistent with the Galactic metal-poor stars.

We note that we have not accounted for possible non-local thermodynamic equilibrium (NLTE) and three-dimensional (3D) effects (M. Asplund 2005; K. Lind et al. 2011) in the present analysis. These effects are not expected to alter the qualitative classification of the programme stars or the main interpretations based on their abundance patterns (J. Yoon et al. 2016).

5.4 Kinematic analysis

In order to know the galactic population to which the programme stars belong, we performed a kinematic analysis of the stars. We followed the procedure described in M. Purandardas et al. (2019) and P. P. Goswami et al. (2021). We calculated the components of space velocities ($U_{\rm LSR}$, $V_{\rm LSR}$, $W_{\rm LSR}$) with respect to local standard of rest (LSR). The values of the parallaxes (π) and proper motions (μ_α, μ_δ) are taken from the Gaia database. Radial velocities of the programme stars are taken from our estimates. V_{spa} ($=\sqrt{U_{\rm LSR}^2 + V_{\rm LSR}^2 + W_{\rm LSR}^2}$) gives the total space velocity. We have calculated the probabilities of the programme stars being in the thin-disc ($P_{\rm thin}$), thick-disc ($P_{\rm thick}$) or halo ($P_{\rm halo}$) population using

[4]*linemake* contains laboratory atomic data (transition probabilities, hyperfine and isotopic substructures) published by the Wisconsin Atomic Physics and the Old Dominion Molecular Physics groups. These lists and accompanying line list assembly software have been developed by C. Sneden and are curated by V. Placco at https://github.com/vmplacco/linemake.

Table 4. Equivalent widths (in mÅ) of lines used for determination of atmospheric parameters and elemental abundances.

Wavelength (Å)	Element	E_{low} (eV)	log *gf*	HE 0401−0138	HE 1246−1344	HE 1153−0518
4045.81	Fe I	1.48	0.280	101.3 (4.10)	–	–
4198.30		2.40	−0.719	–	46.2 (4.16)	–
4202.03		1.48	−0.708	–	78.6 (3.85)	–
4233.60		2.48	−0.604	–	33.6 (3.87)	–
4250.79		1.56	−0.710	64.9 (3.82)	–	–

Note. The numbers in the parentheses in columns 5–7 give the derived abundances from the respective line.

Table 5. Derived atmospheric parameters of our programme stars and literature values.

Star name	T_{eff} (K)	log *g* (cgs)	ξ (km s^{-1})	[Fe I/H]	[Fe II/H]	[Fe/H]	Ref
HE 0401−0138	4830	1.30	0.87	−3.46 ± 0.14	−3.43 ± 0.06	−3.45	1
	4866	1.76	1.45	–	–	−3.34	2
	4929	–	–	–	–	–	3
	5000	2.5	–	–	–	− 4.0	5
HE 1153−0518	4700	0.20	1.47	−3.07 ± 0.20	−3.08 ± 0.16	−3.08	1
	4543	2.18	–	–	–	+0.52	4
	4750	0.0	–	–	–	−4.0	5
HE 1246−1344	4780	1.00	1.22	−3.51 ± 0.09	−3.48 ± 0.01	−3.50	1
	4853	1.65	1.84	–	–	−3.40	2
	4852	–	–	–	–	–	3
	5000	0.5	–	–	–	−4.0	5

References: 1. This work, spectroscopic, 2. P. S. Barklem et al. (2005), 3. Gaia Collaboration (2018), 4. Gaia Collaboration et al. (2023), 5. This work, SED fitting

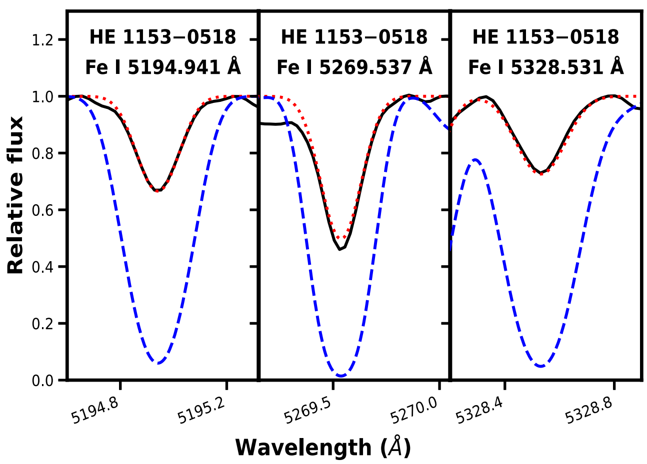

Figure 3. Spectrum synthesis plots of Fe I 5194 Å, 5269 Å, and 5328 Å lines for the object HE 1153 − 0518. The solid lines represent the observed spectra. The dotted lines show the synthesized spectra computed using the atmospheric parameters derived in this study. The dashed lines correspond to the synthesized spectra obtained using the atmospheric parameters reported by Gaia Collaboration (2023).

the procedures given in B. E. Reddy, D. L. Lambert & C. Allende Prieto (2006), T. Bensby, S. Feltzing & I. Lundström (2003, 2004), and T. V. Mishenina et al. (2004).

For HE 0401−0138 and HE 1246−1344, the parallaxes from *Gaia* were used directly. However, for HE 1153−0518, the *Gaia* parallax is negative and unreliable. Therefore, we estimated the distance of this star using the method and equations discussed in M. Purandardas et al. (2019). We assumed a stellar mass of 0.8 $M_\odot$ and used the value of A_V from E. F. Schlafly & D. P. Finkbeiner (2011). We adopted a bolometric correction of BC = −0.48, a value supported by the calibration of A. Alonso et al. (1999) for cool giant stars. Using the estimated distance, we calculated the kinematic parameters for HE 1153−0518 in the same way as for the other two stars.

The values of U_{LSR}, V_{LSR}, W_{LSR}, V_{spa}, P_{thin}, P_{thick}, and P_{halo} for all three programme stars are presented in Table 8.

6 DISCUSSIONS

In this section, we discuss the implications of the derived abundance patterns of the programme stars. We aim to understand the possible formation scenarios of these stars using well-established abundance diagnostics and comparisons with previous studies.

6.1 Classification of the programme stars

Based on the standard classification scheme of EMP stars ([Fe/H] < −3.0; T. C. Beers & N. Christlieb (2005); A. Frebel (2018)), all three programme stars are classified as EMP stars. Among them, HE 0401−0138 and HE 1246−1344 exhibit no carbon enhancement and show abundance patterns typical of normal EMP halo stars, characterized by mild α-element enhancement and low neutron-capture element abundances (Fig. 5). P. S. Barklem et al. (2005) also studied these two objects and reported the abundances of a few elements. For the elements common in both the studies our derived abundances closely match with that of P. S.

Table 6. Elemental abundances in HE 0401−0138 and HE 1246−1344.

			HE 0401−0138				HE 1246−1344			
	Z	Solar log*ε*[a]	log*ε* (dex)	[X/H]	[X/Fe]	[X/Fe][b]	log*ε* (dex)	[X/H]	[X/Fe]	[X/Fe][b]
Li	3	1.05	< 0.80	< −0.25	< +3.20		< 0.30	< −0.75	< +2.75	–
C (CH, 4310 Å)	6	8.43	5.27 (syn)	−3.16	+0.29	+0.24	4.95 (syn)	−3.48	+0.02	−0.06
O	8	8.69	< 6.80 (1)	< −1.89	< +1.56		< 6.58 (1)	<−2.11	< +1.39	–
Na I	11	6.24	3.07±0.19 (2)	−3.17	+0.28	–	4.27±0.02 (2)	−1.97	+1.53	–
Mg I	12	7.60	5.01±0.12 (3)	−2.59	+0.86	+0.42	4.83±0.20 (2)	−2.77	+0.73	+0.50
Ca I	20	6.34	3.41±0.02 (3)	−2.93	+0.52	+0.35	3.35±0.14 (7)	−2.99	+0.51	+0.39
Sc II*	21	3.15	−0.05±0.05 (2)	−3.20	+0.25	+0.11	−0.10±0.14 (2)	−3.25	+0.25	+0.35
Ti I	22	4.95	1.84±0.09 (3)	−3.11	+0.34	+0.28	1.84±0.05 (2)	−3.11	+0.39	+0.25
Ti II	22	4.95	1.99±0.23 (6)	−2.96	+0.49	–	1.86±0.10 (12)	−3.09	+0.41	–
Cr I	24	5.64	2.14±0.08 (2)	−3.50	−0.05	−0.46	1.87±0.17 (4)	−3.77	−0.27	−0.45
Mn I*	25	5.43	1.27±0.03 (2)	−4.16	−0.71	−0.80	1.12±0.08 (2)	−4.31	−0.81	−0.91
Fe I	26	7.50	4.04±0.14 (33)	−3.46	–	–	3.99±0.09 (43)	−3.51	–	–
Fe II	26	7.50	4.07±0.06 (4)	−3.43	–	–	4.02±0.01 (2)	−3.48	–	–
Co I	27	4.99	1.76 (1)	−3.23	+0.22	+0.24	1.62 (1)	−3.37	+0.13	+0.12
Ni I	28	6.22	2.89 (1)	−3.33	+0.12	+0.02	2.80±0.09 (2)	−3.42	+0.08	−0.01
Sr II	38	2.87	−0.39 (1)	−3.24	+0.21	+0.11	−1.70±0.11 (2)	−4.57	−1.07	−1.25
Y II	39	2.21	−0.90 (1)	−3.11	+0.34	+0.05	–	–	–	–
Ba II*	56	2.18	−1.39±0.01 (2)	−3.57	−0.12	−0.21	−2.80 (1)	−4.98	−1.48	–
La II*	57	1.10	<−1.90±0.10 (2)	<−3.00	< +0.45	–	<−1.90±0.10 (2)	<−3.00	< +0.50	–
Ce II*	58	1.58	<−1.24±0.16 (2)	<−2.82	< +0.63	–	<−1.58 (1)	<−3.16	< +0.34	–
Pr II*	59	0.72	<−2.15±0.05 (2)	<−2.87	< +0.58	–	<−1.82±0.10 (2)	<−2.54	< +0.96	–
Nd II*	60	1.42	<−2.10±0.10 (2)	<−3.52	< -0.07	–	<−2.05±0.05 (2)	<−3.47	< +0.03	–
Sm II*	62	0.96	<−2.36 (1)	<−3.32	< +0.13	–	<−1.87±0.24 (3)	<−2.83	< +0.67	–
Eu II*	63	0.52	<−2.20±0.10 (2)	<−2.72	< +0.73	–	<−2.35±0.15 (2)	<−2.87	< +0.63	-

Notes. *Abundance is derived using spectrum synthesis calculations. The number inside the parenthesis shows the number of lines used for the abundance determination.
References: [a] M. Asplund et al. (2009), [b]P. S. Barklem et al. (2005).

Table 7. Elemental abundances in HE 1153−0518.

	Z	Solar log*ε*[a]	log*ε* (dex)	[X/H]	[X/Fe]
Li	3	1.05	< 0.90	< −0.15	< +2.93
C (C_2, 5165 Å)	6	8.43	8.20 (syn)	−0.23	+2.85
C (C_2, 5635 Å)	6	8.43	8.22 (syn)	−0.21	+2.87
O	8	8.69	< 6.89 (syn)	< −1.80	< +1.28
Na I	11	6.24	5.28±0.11 (2)	−0.96	+2.12
Mg I	12	7.60	5.57±0.05 (2)	−2.03	+1.05
Ca I	20	6.34	3.92 (1)	−2.42	+0.66
Sc II*	21	3.15	−0.07 (1)	−3.22	−0.15
Ti I	22	4.95	2.56 (1)	−2.39	+0.69
Ti II	22	4.95	2.33±0.16 (4)	−2.62	+0.46
Cr I	24	5.64	2.70 (1)	−2.94	+0.14
Fe I	26	7.50	4.43±0.20 (16)	−3.07	–
Fe II	26	7.50	4.42±0.16 (2)	−3.08	–
Ni I	28	6.22	3.35 (1)	−2.87	+0.21
Y II	39	2.21	−0.89 (1)	−3.10	−0.02
Ba II*	56	2.18	-1.0±0.17 (3)	−3.18	-0.10
La II*	57	1.10	< −1.40 (1)	<−2.50	< +0.58
$^{12}C/^{13}C = 2.0$					

Notes. *Abundance is derived using spectrum synthesis calculations. The number inside the parenthesis shows the number of lines used for the abundance determination.
[a] M. Asplund et al. (2009).

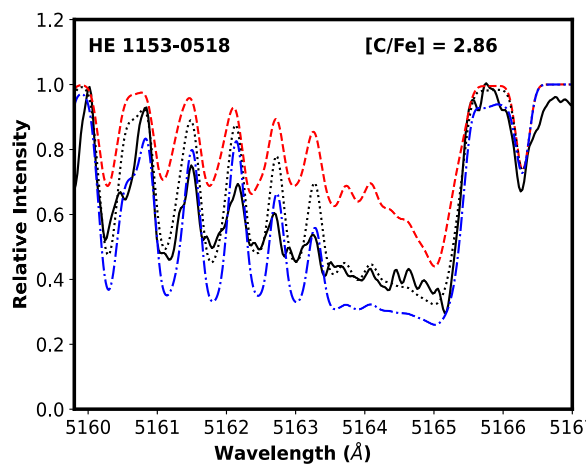

Figure 4. Spectrum synthesis plot of C_2 molecular band around 5165 Å. The solid line represents the observed spectra. The dotted line shows the synthesized spectra. Other two synthesized spectra are displayed corresponding to Δ[C/Fe] = −0.3 and +0.3 with dashed and dash–dotted lines, respectively.

Barklem et al. (2005). In addition to the elements reported by P. S. Barklem et al. (2005), we derived the abundance of sodium for the objects. We also derived the upper limits of the abundances of Li, O, La, Ce, Nd, Pr, Sm, and Eu. The probability estimates support the inclusion of these two objects in the halo population.

The moderate enhancement of the *α*-elements ([(Mg, Ca, Ti)/Fe] ∼ +0.34 to +0.86) in the EMP stars HE 0401−0138

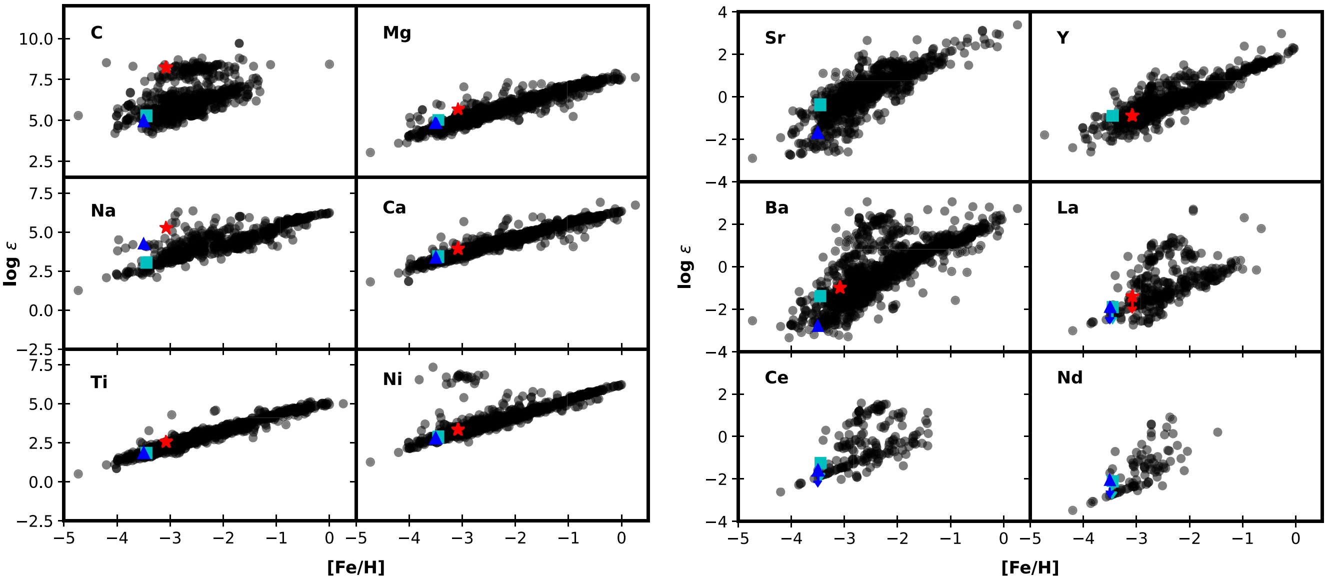

(a) Light elements (b) Heavy elements

Figure 5. Comparison of the observed abundances of a few light and heavy elements of our programme stars with the literature data of metal-poor stars compiled by A. Frebel (2010). The filled circles represent the literature abundance values of metal-poor stars. Filled squares represent HE 0401 − 0138, filled triangles represent HE 1246 − 1344 and filled stars represent HE 1153 − 0518. The error bars to the abundances of the corresponding elements are not visible in the plots as the marker sizes are larger than the error bars.

Table 8. Spatial velocity and probability estimates.

Star name	U_{LSR} (km s^{-1})	V_{LSR} (km s^{-1})	W_{LSR} (km s^{-1})	V_{spa} (km s^{-1})	P_{thin}	P_{thick}	P_{halo}
HE 0401−0138	−57.84 ± 2.87	−256.53 ± 48.18	54.79 ± 16.90	268.61 ± 42.95	0.00	0.00	1.00
HE 1153−0518	−297.30 ± 157.76	−360.34 ± 165.75	−133.06± 99.83	485.73 ± 348.21	0.00	0.00	1.00
HE 1246−1344	27.87 ± 6.73	−475.47 ± 271.18	−273.19 ± 199.48	549.08 ± 332.01	0.00	0.00	1.00

and HE 1246−1344 is consistent with enrichment dominated by core-collapse supernovae of massive stars, as commonly observed in EMP stars (e.g. R. Cayrel et al. (2004)). The low abundances of Fe-peak elements such as Mn further support this picture, as Mn is known to be underproduced in low-metallicity supernovae (R. Cayrel et al. 2004; C. Kobayashi et al. 2006). We note that HE 1246–1344 shows a higher sodium abundance compared to HE 0401–0138. Such star-to-star variations in light odd-Z elements, particularly sodium, are commonly observed among EMP halo stars and do not necessarily imply different formation channels. The sodium yield in core-collapse supernovae is known to be sensitive to progenitor mass, explosion energy, and fallback efficiency, as well as to the degree of mixing in the ejecta (e.g. C. Kobayashi et al. 2006; K. Nomoto, C. Kobayashi & N. Tominaga 2013).

HE 1153−0518, on the other hand, shows very large carbon enhancement ([C/Fe] = +2.86) and low abundances of neutron-capture elements ([(Y, Ba)/Fe] < 0.0). According to the classification criteria of CEMP stars (T. C. Beers & N. Christlieb 2005; A. Frebel 2018; C. J. Hansen et al. 2019), HE 1153−0518 is a bona fide CEMP-no star. Table 9 presents the ratios of a few key elements and the classification of the programmes stars. In the following subsections we will discuss the findings about HE 1153−0518 in detail.

6.2 Position of HE 1153−0518 on the Yoon–Beers diagram and its Group IV membership

Fig.6 shows the location of HE 1153−0518 in the Yoon–Beers A(C)−[Fe/H] diagram. The star has A(C) ≈ 8.2 at [Fe/H] = −3.08 and therefore lies in the high-A(C) region.

Recently, Y. S. Lee et al. (2025) identified a new morphological group of CEMP stars, which they designated as Group IV. These stars are characterized by high absolute carbon abundances (A(C) > 7.39) and low metallicities ([Fe/H] ≤ −3.1), but they lack significant neutron-capture element enhancements and are therefore classified as CEMP-no stars. HE 1153−0518 satisfies all these criteria and thus belongs to the newly proposed Group IV.

Y. S. Lee et al. (2025) suggested that Group IV stars may have formed in relatively carbon-normal metal-poor environments and later acquired additional carbon through mass transfer from an AGB companion in a binary system. The high binary fraction (∼ 30 per cent) they reported supports this scenario. The properties of HE 1153−0518, in particular its extreme sodium enhancement ([Na/Fe] = +2.12), very low carbon isotopic ratio ($^{12}C/^{13}C = 2.0$), and the presence of circumstellar dust, provide further observational constraints on the origin of Group IV stars.

We also note that J. Hong et al. (2026) have recently identified a substantial number of additional Group IV candidates using

Table 9. Classification of the programme stars.

Star name	[Fe/H]	[C/Fe]	[Ba/Fe]	[La/Fe]	[Eu/Fe]	[Ba/Eu]	[La/Eu]	Classification
HE 0401−0138	−3.45	+0.29	−0.12	< +0.45	< +0.73	> −0.85	> −0.28	EMP
HE 1153−0518	−3.08	+2.86	−0.10	< +0.58	–	–	–	CEMP-no
HE 1246−1344	−3.50	+0.02	−1.48	< +0.50	< +0.63	> −2.11	> −0.13	EMP

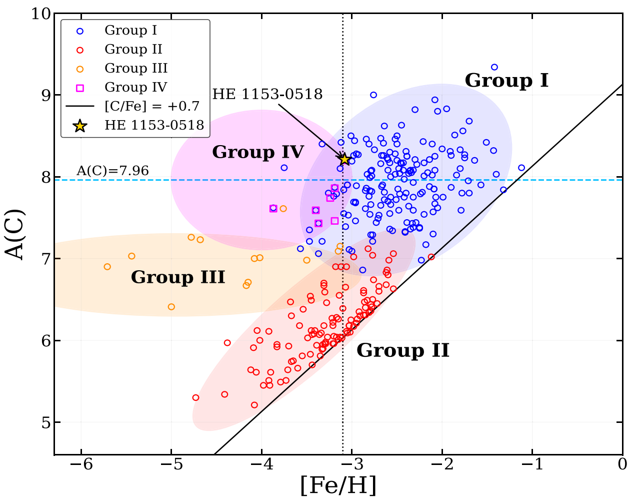

Figure 6. Yoon–Beers diagram showing the absolute carbon abundance, A(C), as a function of metallicity, [Fe/H], for CEMP stars. Blue circles, red circles, orange circles, and magenta squares represent Groups I, II, III, and IV, respectively. The large yellow star marks HE 1153 − 0518 from this work. The coloured ellipses show the approximate locations of the different groups, following J. Yoon et al. (2016) for Groups I–III and Y. S. Lee et al. (2025) for Group IV. The sample includes the full compilation from J. Yoon et al. (2016) together with the stars explicitly listed in Y. S. Lee et al. (2025) and J. Hong et al. (2026). The cyan dashed horizontal line at A(C) = 7.96 marks the high-carbon peak identified by J. Yoon et al. (2016). The vertical dotted line at [Fe/H] = −3.1 approximately marks the metallicity region associated with Group IV. The solid black line represents the CEMP classification boundary corresponding to [C/Fe] = +0.7.

photometric data from the J-PLUS and S-PLUS surveys, indicating that this population is more common than previously recognized.

6.3 Abundance pattern and nucleosynthetic constraints

In addition to carbon enhancement, HE 1153−0518 exhibits extreme sodium enrichment ([Na/Fe] $\sim +2.1$), mild α-element enhancement, low manganese, and very low neutron-capture element abundances. Such a combination is difficult to reproduce through classical AGB nucleosynthesis, which is generally accompanied by significant s-process enrichment (A. I. Karakas & J. C. Lattanzio 2014).

The [Na/Fe] (= +2.12) abundance ratio is among the highest reported for CEMP-no stars at [Fe/H] ≈ -3.1 and may therefore provide an important additional constraint on the progenitor mass and explosion energy in faint supernova models (C. Kobayashi et al. 2006; K. Nomoto et al. 2013).

Rapidly rotating massive stars (spinstars) have been proposed as possible progenitors of some CEMP-no stars (G. Meynet, S. Ekström & A. Maeder 2006; G. Meynet et al. 2010; U. Frischknecht, R. Hirschi & F.-K. Thielemann 2012; A. Maeder & G. Meynet 2015; U. Frischknecht et al. 2016; A. Choplin et al. 2017); however, spinstar models typically predict enhanced light *s*-process elements, leading to elevated Sr and Y abundances (U. Frischknecht et al. 2016), which are not observed in HE 1153−0518. In contrast, models of faint core-collapse supernovae with mixing and fallback naturally explain the observed pattern of high [C/Fe] and [Na/Fe], low [Fe/H], and low neutron-capture element abundances (H. Umeda & K. Nomoto 2003; K. Nomoto et al. 2013).

While enrichment by faint core-collapse supernovae remains a viable formation channel for HE 1153−0518, its placement in the newly proposed Group IV also allows the possibility that binary mass transfer has contributed to its observed chemical composition, as discussed in Section 6.2.

6.4 Carbon isotopic ratio, radial-velocity variability, and the role of AGB mass transfer

The carbon isotopic ratio that we derived for HE 1153−0518 is found to be very low ($^{12}C/^{13}C = 2.0$). This value is close to CN-cycle equilibrium and can arise from internal mixing in evolved giants. Similar low isotopic ratios are also observed in some CEMP-*s* and CEMP-*r*/*s* stars and are commonly interpreted as the result of internal mixing operating after the accretion of carbon-rich material from an AGB companion (M. Spite et al. 2006; T. T. Hansen et al. 2015).

From Table 2, we can see that HE 1153−0518 might be a radial velocity variable. So, the binary interaction and mass transfer cannot be excluded a priori. Indeed, J. Yoon et al. (2019), based on the results of T. T. Hansen et al. (2016) and A. Arentsen et al. (2019), noted that a significant fraction of high-A(C) CEMP-no stars are binaries, suggesting that AGB mass transfer may operate for at least some members of this population. This possibility is particularly relevant in the context of Group IV stars, for which Y. S. Lee et al. (2025) have suggested binary mass transfer as a contributing formation channel. However, J. Yoon et al. (2019) also emphasized that binary mass transfer scenario alone cannot simultaneously explain the high carbon abundances and low barium abundances observed in high-A(C) CEMP-no stars. At present, no well-established low-metallicity AGB models can reproduce the observed lack of correlation between A(C) and A(Ba). Thus, while binary interaction with a now extinct AGB may influence the surface composition of HE 1153−0518, it may not be the dominant origin of its carbon enrichment.

6.5 Evolutionary state, lithium, oxygen, and infrared excess

HE 1153−0518 has a very low surface gravity (log g = 0.20), indicating that it is a highly evolved giant. The non-detection of lithium and the resulting upper limits are consistent with such an evolved evolutionary stage and do not place additional constraints on the formation history (K. Lind, M. Asplund & P. S. Barklem 2009). Similarly, the upper limits on oxygen abundance are consistent with those seen in other EMP and CEMP-no stars, and are not decisive enough to distinguish between different early chemical enrichment scenarios (R. Cayrel et al. 2004; M. Spite et al. 2005).

The SED of HE 1153−0518 shows a clear infrared (IR) excess, indicating the presence of circumstellar dust, which is very common for objects with low surface gravity (log g = 0.2). While, such an IR excess might suggest an intrinsic AGB evolutionary phase, the lack of *s*-process enrichment and the very low value of $^{12}C/^{13}C$ are inconsistent with expectations for thermally pulsing AGB stars. Recent studies have demonstrated that dust formation can occur even at extremely low metallicities, particularly in carbon-rich environments, without necessarily requiring classical AGB evolution (M. L. Boyer et al. 2015; P. Ventura et al. 2021). In this context, the infrared excess observed in HE 1153−0518 provides one of the few direct observational indications supporting dust production at [Fe/H] < −3.0.

6.6 Accretion origin and formation scenario

Although the *Gaia* parallax of HE 1153−0518 is negative and unreliable, we have estimated its distance photometrically. The derived kinematic parameters, though carrying large uncertainties, place this star firmly in the halo population with $P_{\rm halo} = 1.00$, which is fully consistent with its extremely low metallicity and CEMP-no chemical abundance pattern.

In this context, HE 1153−0518 may have formed in an early and chemically primitive environment. Such environments are commonly found in small systems like ultra-faint dwarf galaxies or dwarf spheroidal galaxies, which were later accreted by the Milky Way (J. Yoon et al. 2019). However, with the present kinematic data of the star, this origin cannot be confirmed.

The combination of high carbon abundance, strong sodium enhancement, low neutron-capture element abundances, and a carbon isotopic ratio close to CN-cycle equilibrium indicates that enrichment by early massive stars, such as faint core-collapse supernovae, may have played an important role. At the same time, the evidence for binarity and the presence of IR excess suggests that mass transfer from an AGB companion and internal mixing could also have influenced the observed surface abundances. The location of this star in the newly proposed Group IV further supports the possibility that binary interaction may have contributed to its chemical composition. Further observations, particularly long-term radial-velocity monitoring and improved astrometric data, will be required to better distinguish between these possible formation and enrichment scenarios.

7 CONCLUSIONS

We have performed detailed high-resolution spectroscopic analysis on three stars: HE 0401−0138, HE 1153−0518, and HE 1246−1344. All three programme stars are found to be EMP stars with the [Fe/H] range from −3.08 to −3.50.

(i) The stars HE 0401−0138 and HE 1246−1344 show chemical abundance patterns typical of normal EMP halo stars, including moderate α-element enhancement and low neutron-capture element abundances, consistent with enrichment by early core-collapse supernovae. HE 1153−0518 is identified as a newly discovered CEMP-no star belonging to the recently proposed Group IV. This star shows very high absolute carbon abundance, very low neutron-capture element abundances, and extreme sodium enhancement.

(ii) The abundance pattern of HE 1153−0518, including extreme sodium enhancement, low neutron-capture elements, and a very low carbon isotopic ratio, suggests that its chemical composition reflects enrichment by material processed through early nucleosynthetic channels. While enrichment by early massive stars, such as faint core-collapse supernovae, provides a natural explanation for several of the observed features, the presence of radial-velocity variability indicates that binary interaction with a now extinct AGB and internal mixing may also have played a role in creating the observed surface abundances.

(iii) Although the *Gaia* parallax of HE 1153−0518 is negative and hence not usable directly, we have estimated its distance using a photometric method. The kinematic parameters derived from this estimated distance confirm that HE 1153−0518 belongs to the Galactic halo population, consistent with its extremely low metallicity and chemical abundance pattern typical of CEMP-no stars found in the halo. An origin in a small, chemically primitive system such as an ultra-faint dwarf or dwarf spheroidal galaxy, later accreted by the Milky Way, remains a plausible explanation.

The discovery and detailed comprehensive study of HE 1153−0518 add an important new object to the limited sample of high-A(C) CEMP-no stars. Its unusual combination of strong carbon enhancement, extreme sodium abundance, low neutron-capture element content, low carbon isotopic ratio, and infrared excess makes it a valuable probe for understanding the diversity of early chemical enrichment pathways and the nature of the first generations of stars.

ACKNOWLEDGEMENTS

This work made use of the SIMBAD astronomical database, operated at CDS, Strasbourg, France, the NASA ADS, USA and data from the European Space Agency (ESA) mission *Gaia* (https://www.cosmos.esa.int/gaia), processed by the Gaia Data Processing and Analysis Consortium (DPAC, https://www.cosmos.esa.int/web/gaia/dpac/consortium). This publication makes use of VOSA, developed under the Spanish Virtual Observatory (https://svo.cab.inta-csic.es) project funded by MCIN/AEI/10.13039/501100011033/ through grant PID2020-112949GB-I00. VOSA has been partially updated by using funding from the European Union's Horizon 2020 Research and Innovation Programme, under Grant Agreement no. 776403 (EXOPLANETS-A).

This study is based [in part] on data collected at Subaru Telescope, which is operated by the NAOJ. [Part of] the data are retrieved from the JVO portal (http://jvo.nao.ac.jp/portal) operated by the NAOJ.

DATA AVAILABILITY

The spectroscopic data underlying this article were obtained from the Subaru Telescope archive through the JVO portal (http://jvo.nao.ac.jp/portal) operated by the NAOJ. Additional photometric and astrometric data used in this work were obtained from publicly available databases including SIMBAD and *Gaia*. The derived abundance data and other results are included within the article. Additional data products will be shared on reasonable request to the corresponding author.

REFERENCES

Alonso A., Arribas S., Martinez-Roger C., 1996, A&A, 313, 873
Alonso A., Arribas S., Martínez-Roger C., 1999, A&AS, 140, 261
Aoki W., Beers T. C., Christlieb N., Norris J. E., Ryan S. G., Tsangarides S., 2007, ApJ, 655, 492
Arentsen A., Starkenburg E., Shetrone M. D., Venn K. A., Depagne É., McConnachie A. W., 2019, A&A, 621, A108
Asplund M., 2005, ARA&A, 43, 481
Asplund M., Grevesse N., Sauval A. J., Scott P., 2009, ARA&A, 47, 481
Barklem P. S. et al., 2005, A&A, 439, 129
Bayo A., Rodrigo C., Barrado Y Navascués D., Solano E., Gutiérrez R., Morales-Calderón M., Allard F., 2008, A&A, 492, 277
Beers T. C., Christlieb N., 2005, ARA&A, 43, 531
Bensby T., Feltzing S., Lundström I., 2003, A&A, 410, 527
Bensby T., Feltzing S., Lundström I., 2004, A&A, 415, 155
Bonifacio P. et al., 2015, A&A, 579, A28
Boyer M. L. et al., 2015, ApJ, 800, 51
Castelli F., Kurucz R. L., 2003, in Piskunov N., Weiss W. W., Gray D. F., eds, Modelling of Stellar Atmospheres, Vol. 210. p. A20
Cayrel R. et al., 2004, A&A, 416, 1117
Choplin A., Hirschi R., Meynet G., Ekström S., 2017, A&A, 607, L3
Cutri R. M. et al., 2003, VizieR Online Data Catalog, p. II/246
Frebel A., 2010, Astron. Nachr., 331, 474
Frebel A., 2018, Annual Review of Nuclear and Particle Science, 68, 237
Frebel A., Norris J. E., 2015, ARA&A, 53, 631
Frischknecht U., Hirschi R., Thielemann F.-K., 2012, A&A, 538, L2
Frischknecht U. et al., 2016, MNRAS, 456, 1803
Gaia Collaboration, 2018, A&A, 616, A11
Gaia Collaboration, 2023, A&A, 674, A1
Goswami A., Aoki W., Beers T. C., Christlieb N., Norris J. E., Ryan S. G., Tsangarides S., 2006, MNRAS, 372, 343
Goswami A., Aoki W., Karinkuzhi D., 2015, MNRAS, 455, 402
Goswami P. P., Rathour R. S., Goswami A., 2021, A&A, 649, A49
Hansen C. J., Hansen T. T., Koch A., Beers T. C., Nordström B., Placco V. M., Andersen J., 2019, A&A, 623, A128
Hansen T. et al., 2014, ApJ, 787, 162
Hansen T. T., Andersen J., Nordström B., Beers T. C., Yoon J., Buchhave L. A., 2015, A&A, 583, A49
Hansen T. T., Andersen J., Nordström B., Beers T. C., Placco V. M., Yoon J., Buchhave L. A., 2016, A&A, 586, A160
Hinkle K., Wallace L., Valenti J., Harmer D., 2000, Visible and Near Infrared Atlas of the Arcturus Spectrum 3727–9300 A
Honda S., Aoki W., Kajino T., Ando H., Beers T. C., Izumiura H., Sadakane K., Takada-Hidai M., 2004, ApJ, 607, 474
Hong J., Beers T. C., Huang Y., Cabrera Garcia J., Lee Y. S., Placco V. M., Kirby E. N., 2026, preprint (arXiv:2602.10325)
Karakas A. I., Lattanzio J. C., 2014, PASA, 31, e030
Kobayashi C., Umeda H., Nomoto K., Tominaga N., Ohkubo T., 2006, ApJ, 653, 1145
Lee Y. S., Beers T. C., Hirai Y., Hong J., Jeong M., Kim C., Kim Y. K., 2025, ApJ, 991, L42
Lind K., Asplund M., Barklem P. S., 2009, A&A, 503, 541
Lind K., Asplund M., Barklem P. S., Belyaev A. K., 2011, A&A, 528, A103
Lucey M. et al., 2023, MNRAS, 523, 4049
Maeder A., Meynet G., 2015, A&A, 580, A32
Meynet G., Ekström S., Maeder A., 2006, A&A, 447, 623
Meynet G., Hirschi R., Ekstrom S., Maeder A., Georgy C., Eggenberger P., Chiappini C., 2010, A&A, 521, A30
Mishenina T. V., Soubiran C., Kovtyukh V. V., Korotin S. A., 2004, A&A, 418, 551
Noguchi K. et al., 2002, PASJ, 54, 855
Nomoto K., Kobayashi C., Tominaga N., 2013, ARA&A, 51, 457
Norris J. E. et al., 2013, ApJ, 762, 28
Purandardas M., Goswami A., 2021, ApJ, 912, 74
Purandardas M., Goswami A., Goswami P. P., Shejeelammal J., Masseron T., 2019, MNRAS, 486, 3266
Rani S., Pandey G., Subramaniam A., Chung C., Sahu S., Kameswara Rao N., 2021, ApJ, 923, 162
Reddy B. E., Lambert D. L., Allende Prieto C., 2006, MNRAS, 367, 1329
Ren J., Christlieb N., Zhao G., 2012, A&A, 537, A118
Rossi S., Beers T. C., Sneden C., Sevastyanenko T., Rhee J., Marsteller B., 2005, AJ, 130, 2804
Schlafly E. F., Finkbeiner D. P., 2011, ApJ, 737, 103
Shejeelammal J., Goswami A., 2024, MNRAS, 527, 2323
Sneden C. A., 1973, PhD thesis, Univ. Texas at Austin
Spite M. et al., 2005, A&A, 430, 655
Spite M. et al., 2006, A&A, 455, 291
Spite M., Caffau E., Bonifacio P., Spite F., Ludwig H. G., Plez B., Christlieb N., 2013, A&A, 552, A107
Umeda H., Nomoto K., 2003, Nature, 422, 871
Valenti J. A., Piskunov N., 1996, A&AS, 118, 595
Ventura P. et al., 2021, A&A, 655, A6
Yoon J. et al., 2016, ApJ, 833, 20
Yoon J., Beers T. C., Tian D., Whitten D. D., 2019, ApJ, 878, 97
Zhang L., Karlsson T., Christlieb N., Korn A. J., Barklem P. S., Zhao G., 2011, A&A, 528, A92

APPENDIX A:

Table A1. Equivalent widths (in mÅ) of lines used for calculation of elemental abundances.

Wavelength (Å)	Element	E_{low} (eV)	log *gf*	HE 0401−0138	HE 1246−1344	HE 1153−0518
4045.81	Fe I	1.48	0.280	101.3 (4.10)	–	–
4198.30		2.40	−0.719	–	46.2 (4.16)	–
4202.03		1.48	−0.708	–	78.6 (3.85)	–
4233.60		2.48	−0.604	–	33.6 (3.87)	–
4250.79		1.56	−0.710	64.9 (3.82)	–	–
4271.76		1.48	−0.164	–	102.1 (4.01)	–
4375.93		0.00	−3.031	59.9 (3.98)	–	–
4383.55		1.48	0.200	96.9 (3.86)	114.5 (3.94)	–
4404.75		1.56	−0.142	88.9 (4.02)	97.8 (3.86)	–
4415.12		1.61	−0.615	73.7 (4.03)	87.8 (4.10)	–
4427.31		0.05	−3.044	68.8 (4.31)	62.2 (3.84)	–
4442.34		2.20	−1.255	21.5 (3.93)	35.2 (4.18)	–
4447.72		2.22	−1.342	24.8 (4.13)	–	–
4466.573		0.11	−4.464	–	–	–
4528.61		2.18	−0.822	–	41.0 (3.83)	–
4602.94		1.48	−1.950	–	–	–
4871.32		2.87	−0.410	–	31.1 (4.00)	–
4872.14		2.88	−0.600	–	22.3 (3.99)	–
4890.76		2.88	−0.430	–	31.4 (4.03)	–
4891.49		2.85	−0.140	42.5 (4.05)	48.5 (4.05)	–
4918.99		2.87	−0.370	34.0 (4.09)	28.5 (3.90)	–
4920.50		2.83	0.060	46.7 (3.92)	49.7 (3.85)	71.2 (4.12)
4982.50		4.10	0.164	–	–	–
4994.13		0.92	−3.080	–	–	–
5006.12		2.83	−0.615	–	22.6 (3.94)	–
5041.76		1.48	−2.203	–	32.2 (4.11)	–
5049.82		2.28	−1.420	–	19.9 (4.02)	–
5051.64		0.91	−2.795	30.3 (4.05)	31.6 (3.98)	85.3 (4.74)
5083.34		0.96	−2.958	21.4 (4.05)	20.9 (3.96)	–
5166.28		0.00	−4.195	16.6 (3.93)	–	–
5171.60		1.49	−1.793	44.2 (4.06)	44.6 (3.94)	–
5192.34		3.00	−0.421	–	21.8 (3.91)	57.6 (4.51)
5194.94		1.56	−2.090	–	37.7 (4.19)	71.0 (4.60)
5202.34		2.18	−1.838	11.6 (4.07)	–	–
5216.27		1.61	−2.150	–	28.0 (4.11)	56.4 (4.47)
5217.39		3.21	−1.162	–	–	–
5226.86		3.04	−0.555	17.5 (4.02)	–	–
5227.19		1.56	−1.228	72.8 (4.25)	72.3 (3.98)	108.5 (4.47)
5232.94		2.94	−0.190	35.5 (4.00)	33.6 (3.88)	70.6 (4.44)
5242.49		3.63	−0.840	–	–	–
5266.56		3.00	−0.490	21.4 (4.03)	21.2 (3.96)	39.1 (4.25)
5269.54		0.86	−1.321	85.7 (3.81)	105.8 (3.95)	133.7 (4.19)
5270.36		1.61	−1.510	62.1 (4.32)	64.1 (4.15)	95.8 (4.53)
5281.79		3.04	−1.020	14.1 (4.37)	–	–
5283.62		3.24	−0.630	–	–	38.8 (4.67)
5324.18		3.21	−0.240	20.2 (3.98)	20.9 (3.95)	–
5328.04		0.91	−1.466	83.2 (3.93)	103.3 (4.06)	123.2 (4.11)
5328.53		1.56	−1.850	36.6 (4.02)	44.0 (4.05)	75.3 (4.40)
5341.02		1.61	−2.060	–	28.5 (4.02)	–
5446.92		0.99	−1.930	–	77.6 (4.01)	–
5455.61		1.01	−2.091	64.8 (4.17)	67.4 (4.00)	119.3 (4.74)
5497.52		1.01	−2.849	24.5 (4.04)	27.9 (4.03)	–
5501.47		0.96	−2.950	–	18.7 (3.84)	–
5506.78		0.99	−2.797	32.8 (4.16)	29.8 (3.99)	44.7 (4.09)
5572.84		3.40	−0.310	15.5 (4.11)	13.8 (4.00)	–
5586.76		3.37	−0.210	–	18.3 (4.01)	–
5615.64		3.33	−0.140	–	24.6 (4.06)	–
6136.61		2.45	−1.400	9.7 (3.80)	–	–
6230.72		2.56	−1.281	–	–	–

Table A1 – *continued*

Wavelength (Å)	Element	E_{low} (eV)	log *gf*	HE 0401−0138	HE 1246−1344	HE 1153−0518
6335.33		2.20	−2.230	–	–	15.8 (4.38)
6494.98		2.40	−1.273	21.0 (3.99)	21.6 (3.94)	–
4233.17	Fe II	2.58	−2.000	21.0 (4.01)	–	–
4555.89		2.83	−2.290	–	10.5 (4.01)	–
4583.84		2.81	−2.020	–	–	–
4923.93		2.89	−1.320	37.3 (4.14)	–	67.7 (4.30)
5018.44		2.89	−1.220	36.9 (4.04)	–	–
5197.58		3.23	−2.100	6.1 (4.10)	–	27.9 (4.53)
5234.62		3.22	−2.050	–	7.7 (4.02)	–
5276.00		3.20	−1.940	–	–	–
5889.95	Na I	0.00	0.117	93.1 (3.20)	146.6 (4.26)	244.5 (5.20)
5895.92		0.00	−0.184	71.5 (2.94)	133.0 (4.28)	225.2 (5.36)
4571.10	Mg I	0.00	−5.691	–	16.7 (4.68)	–
5172.68		2.71	−0.402	114.6 (5.01)	–	156.5 (5.58)
5183.60		2.72	−0.180	132.1 (5.14)	–	169.5 (5.55)
5528.40		4.35	−0.620	26.6 (4.89)	31.0 (4.97)	–
4226.73	Ca I	0.00	0.243	–	108.3 (3.42)	–
4283.01		1.89	−0.224	–	–	–
4302.53		1.90	0.275	–	32.7 (3.29)	–
4318.65		1.90	−0.208	19.4 (3.41)	16.7 (3.31)	–
4434.96		1.89	−0.029	–	28.2 (3.44)	–
4454.78		1.90	0.252	–	36.9 (3.38)	–
5588.75		2.53	0.210	–	17.8 (3.52)	–
5594.46		2.52	−0.050	–	–	–
5857.45		2.93	0.230	–	–	19.4 (3.92)
6102.72		1.88	−0.890	–	–	–
6122.22		1.89	−0.409	19.0 (3.43)	–	–
6162.17		1.90	0.100	–	–	–
6439.07		2.53	0.470	22.7 (3.38)	14.0 (3.07)	–
4533.24	Ti I	0.85	0.476	14.0 (1.84)	–	–
4981.73		0.85	0.504	13.7 (1.75)	16.0 (1.81)	–
4991.06		0.84	0.380	–	–	–
4999.50		0.83	0.250	–	11.9 (1.88)	–
5007.21		0.82	0.112	–	–	–
5192.97		0.02	−1.006	7.1 (1.93)	–	28.5 (2.56)
4028.34	Ti II	1.89	−1.000	–	–	–
4290.22		1.16	−1.120	52.4 (2.24)	45.6 (1.79)	–
4300.05		1.18	−0.770	–	–	–
4312.86		1.18	−1.160	–	–	–
4395.03		1.08	−0.660	–	72.2 (2.03)	–
4417.72		1.16	−1.430	–	40.1 (1.92)	–
4443.79		1.08	−0.700	63.5 (2.09)	69.1 (1.94)	90.1 (2.23)
4444.56		1.12	−2.030	8.8 (1.63)	–	–
4450.48		1.08	−1.450	–	35.4 (1.73)	–
4468.51		1.13	−0.600	–	64.1 (1.72)	–
4470.86		1.16	−2.280	8.2 (1.88)	–	–
4501.27		1.12	−0.750	63.6 (2.17)	63.6 (1.83)	–
4533.97		1.24	−0.770	–	61.6 (1.93)	–
4563.76		1.22	−0.960	47.6 (1.91)	58.6 (1.99)	–
4571.97		1.57	−0.530	–	–	–
4589.96		1.24	−1.790	–	22.6 (1.91)	–
4779.98		2.05	−1.370	–	–	38.7 (2.54)
4805.09		2.06	−1.100	–	–	–
4865.61		1.12	−2.610	–	–	19.5 (2.18)
5129.15		1.89	−1.390	–	–	–
5185.91		1.89	−1.350	–	–	–
5188.68		1.58	−1.210	–	29.1 (1.82)	–
5226.54		1.57	−1.300	–	23.6 (1.76)	65.1 (2.38)

Table A1 – *continued*

Wavelength (Å)	Element	E_{low} (eV)	log *gf*	HE 0401−0138	HE 1246−1344	HE 1153−0518
4254.34	Cr I	0.00	−0.114	55.4 (2.08)	55.7 (1.88)	–
4274.80		0.00	−0.231	–	45.2 (1.65)	–
4289.72		0.00	−0.361	52.5 (2.20)	54.3 (2.06)	–
5206.04		0.94	0.019	–	27.1 (1.88)	65.0 (2.70)
4092.38	Co I	0.92	−0.940	–	–	–
4118.77		1.05	−0.490	–	14.5 (1.62)	–
4121.31		0.92	−0.320	27.7 (1.76)	–	–
4714.41	Ni I	3.38	0.260	–	5.7 (2.86)	–
5476.90		1.83	−0.890	22.0 (2.89)	18.6 (2.74)	48.4 (3.35)
4077.71	Sr II	0.00	0.167	78.2 (−0.39)	57.0 (−1.62)	–
4215.52		0.00	−0.145	–	46.3 (−1.78)	–
4177.53	Y II	0.41	−0.160	25.9 (−0.90)	–	–
4900.12		1.03	−0.090	–	–	23.3 (−0.89)

Note. The numbers in the parenthesis in columns 5–7 give the derived abundances from the respective line.

This paper has been typeset from a TEX/LATEX file prepared by the author.